

Lossless Monochromator in an Ultrafast Electron Microscope Using Near-Field THz Radiation

Michael Yannai^{1,2,*}, Yuval Adiv^{1,2,*}, Raphael Dahan^{1,2,*}, Kangpeng Wang^{1,2,3}, Alexey Gorlach^{1,2},
Nicholas Rivera^{4,5}, Tal Fishman^{1,2}, Michael Krüger^{2,6}, and Ido Kaminer^{1,2,†}

¹Faculty of Electrical & Computer Engineering, Technion - Israel Institute of Technology, Haifa 3200003, Israel

²Solid State Institute, Technion - Israel Institute of Technology, Haifa 3200003, Israel

³Shanghai Institute of Optics and Fine Mechanics, Chinese Academy of Sciences, Shanghai 201815, China

⁴Department of Physics, Harvard University, Cambridge, Massachusetts 02138, USA

⁵Department of Physics, Massachusetts Institute of Technology, Cambridge, Massachusetts 02139, USA

⁶Department of Physics, Technion - Israel Institute of Technology, Haifa 3200003, Israel



(Received 17 January 2023; revised 3 July 2023; accepted 21 August 2023; published 4 October 2023)

The ability to form monoenergetic electron beams is vital for high-resolution electron spectroscopy and imaging. Such capabilities are commonly achieved using an electron monochromator, which energy filters a dispersed electron beam, thus reducing the electron flux to yield down to meV energy resolution. This reduction in flux hinders the use of monochromators in many applications, such as ultrafast transmission electron microscopes (UTEMs). Here, we develop and demonstrate a mechanism for electron energy monochromation that does not reduce the flux—a lossless monochromator. The mechanism is based on the interaction of free-electron pulses with single-cycle THz near fields, created by nonlinear conversion of an optical laser pulse near the electron beam path inside a UTEM. Our experiment reduces the electron energy spread by a factor of up to 2.9 without compromising the beam flux. Moreover, as the electron-THz interaction takes place over an extended region of many tens of microns in free space, the realized technique is highly robust—granting uniform monochromation over a wide area, larger than the electron beam diameter. We further demonstrate the wide tunability of our method by monochromating the electron beam at multiple primary electron energies from 60 to 200 keV, studying the effect of various electron and THz parameters on its performance. Our findings have direct applications in the fast-growing field of ultrafast electron microscopy, allowing time- and energy-resolved studies of exciton physics, phononic vibrational resonances, charge transport effects, and optical excitations in the mid IR to the far IR.

DOI: [10.1103/PhysRevLett.131.145002](https://doi.org/10.1103/PhysRevLett.131.145002)

Electron energy loss spectroscopy (EELS) [1] is a primary technique in transmission electron microscopy (TEM), used routinely in the chemical and structural analysis of materials down to the atomic scale. A key parameter for determining the achievable spectral resolution in EELS is the spectral width of the probe electron, which sets the width of the zero-loss peak in the electron energy spectrum.

The conventional approach for obtaining a smaller energy spread and hence, higher electron energy resolution, is to incorporate an electron monochromator into the TEM column. This element filters an initially energy-dispersed electron beam, thus achieving energy resolution down to a few meV [2]. The monochromator provides the added value of reducing the chromatic aberration, thereby improving the imaging resolution. However, this approach is extremely lossy, usually removing more than 90% of the incident electron flux. The reduced flux hinders the usage of monochromators in many applications, especially ones *a priori* limited by an inherently low electron current.

The need for high energy resolution is especially acute in the fast-rising field of ultrafast electron microscopy [3–5]. Many ultrafast TEMs (UTEMs) rely on femtosecond light pulses to excite (pump) a sample and then measure (probe) it using femtosecond electron pulses, achieving simultaneous nanometer-femtosecond spatiotemporal resolution [6–19]. In such systems, the electron current is inherently low, inhibiting the use of conventional monochromators.

Progress toward efficient monochromators in the UTEM could enable time-dependent explorations of a wide range of phenomena requiring meV-scale electron energy resolution, such as phonon-polariton [18,20,21], plasmon [22–25], and exciton [26,27] physics, vibrational resonances [28–36], charge transport effects [37–39], and quantum electron optics [40–44]. However, existing monochromation schemes are insufficient for enabling time-dependent studies of such phenomena due to extremely low resulting flux.

Here we realize an optically driven lossless monochromator in a UTEM, and showcase its efficiency and

robustness for a multitude of operating conditions. The underlying mechanism is free-electron interaction with a single-cycle THz near field, which is generated by femto-second laser excitation of a bulk InAs crystal [38]. We show that our technique reduces the energy spread of 80 keV electrons from 0.8 eV to 0.28 eV at full-width half-maximum (FWHM) without losing electrons. The resulting electron beam energy width is the narrowest reported so far in UTEMs (the previous record relied on photo-emission in field emission guns and was reported to be 0.6–1 eV [5,45]).

The wider concept of electron control and shaping using AC electromagnetic fields has been previously studied for various applications, including laser-driven electron acceleration [46] and attosecond electron pulse generation [47]. In the context of GHz- and THz-frequency interactions, efforts so far have focused mostly on temporal manipulations and acceleration schemes. For instance, modulating a continuous electron beam by passing it through a GHz cavity followed by a slit was proposed as a means to generate picosecond [48,49] and more recently femtosecond electron pulses [50–52]. A different scheme involved a laser-driven photoconductive switch in conjunction with a slit [53]. Moreover, in recent years, there has been a growing interest in the use of THz pulses for controlling the electron phase-space distribution and for electron beam metrology. While some studies have investigated the interaction of electron pulses with THz near fields to compress the electron pulse in time [11,54–56], others have exploited THz fields for temporal characterization of electron beams [54,57]. Additionally, single-cycle

THz pulses have been shown to enhance or suppress the photoemission of electrons from a nanostructure [58]. In the field of particle acceleration, several studies have demonstrated THz-driven linear electron accelerators for keV [59] and MeV [60] electron beams. A recent study introduced a THz device capable of accelerating, focusing, and compressing the temporal duration of an electron beam [61]. However, none of the above studies has utilized THz fields to demonstrate electron beam monochromatization.

Furthermore, a recent theoretical work has considered the use of two points of electron-microwave-cavity interaction to achieve energy monochromatization in a UTEM setup [62]. Our work now demonstrates this concept, using just a single point of free-electron-THz interaction, analyzing the interaction efficiency and robustness.

Figure 1 describes the free-electron-THz interaction mechanism and the setup we used for monochromatization of free-electron pulses inside the UTEM (see also Methods). The interaction relies on a pump-probe scheme, in which each femtosecond laser pulse is split into a pump that creates a THz pulse, and a probe that creates an electron pulse. To generate the THz near-field pulse, we irradiate a semiconductor crystal with a femtosecond pump pulse, inducing transient electron and hole currents, which lead to THz generation via the photo-Dember effect [63]. To generate the free-electron probe pulse, the probe laser pulse is up converted to the fourth harmonic and excites the microscope's electron-emitting tip [Fig. 1(a)]. The photo-generated free-electron pulse undergoes dispersion

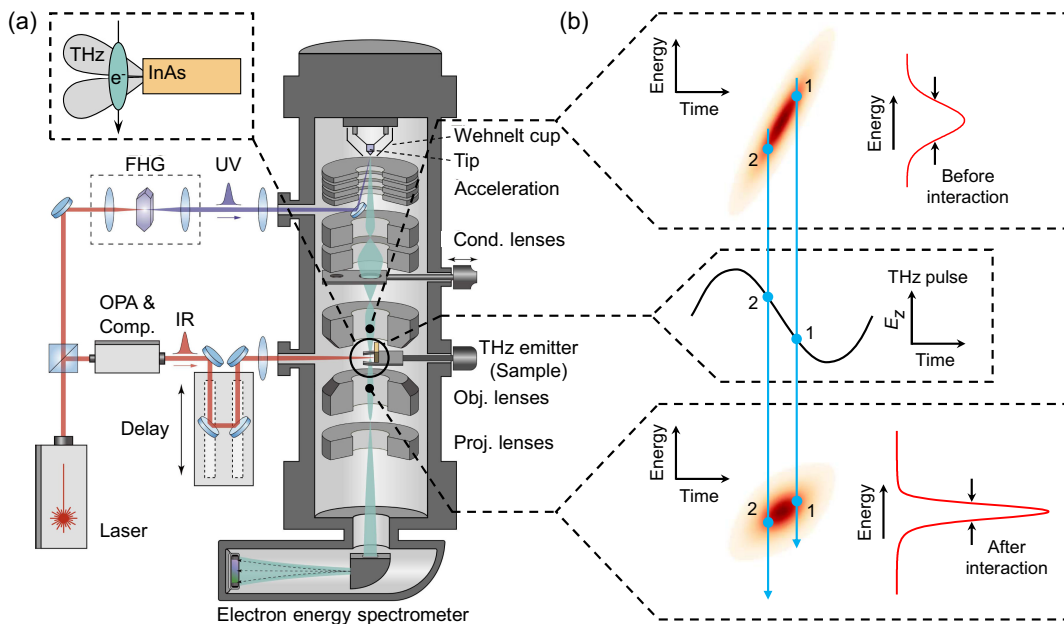


FIG. 1. Electron beam monochromator using near-field THz radiation: setup and concept. (a) Illustration of an UTEM, depicting the pump (IR) and probe (UV) laser paths, and the TEM column. FHG, fourth harmonic generation; OPA, optical parametric amplifier, Comp, laser pulse compressor; Cond, condenser; Obj, objective; Proj, projection. The top-left inset illustrates the electron-THz interaction. For further details see Methods. (b) Illustration of the electron energy spectrum (right, red) and phase-space distribution (left) before and after the interaction with a time-synchronized THz pulse (center panel) conveying the lossless monochromatization process.

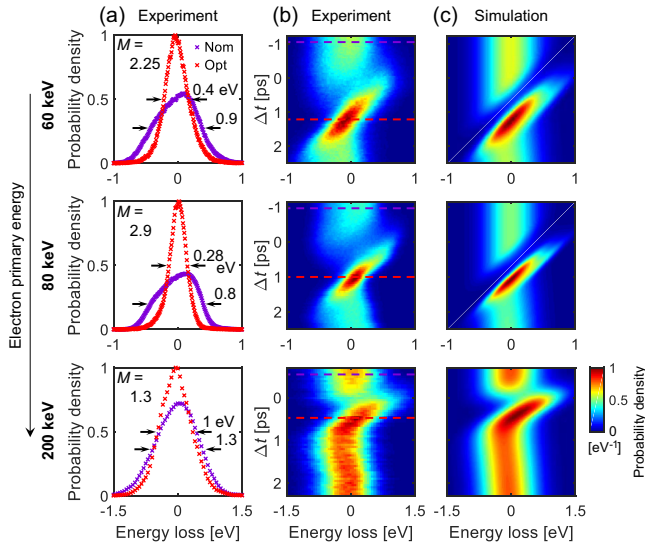


FIG. 2. Analyzing the lossless monochromator operation. (a) Electron energy spectra measured without THz interaction (no monochromation, purple), compared to optimal THz interaction (maximum monochromation, red). Horizontal arrows illustrate the change in the electron energy spread at FWHM. (b) Measured and (c) simulated electron energy spectra versus pump-probe time delay (Δt). The purple and red dashed lines in (b) correspond to the data in (a), given for three electron primary energies (60–200 keV) and for a pump laser pulse energy of 10 nJ (pulse duration of 50 fs with peak intensity of $1.6 \times 10^{10} \text{ W cm}^{-2}$).

during the acceleration process and propagation through the column as illustrated by the phase-space diagram [Fig. 1(b), top panel].

During the interaction between the free electron and the THz field [Fig. 1(b), center panel], different points in the electron phase-space experience different amounts of force exerted by the THz field, modifying the phase space and the resulting energy distribution. Specifically, at an optimal temporal overlap between the electron pulse and the THz pulse, the more energetic part of the electron [Fig. 1(b), point “1”] interacts with a decelerating field while the less energetic part [Fig. 1(b), point “2”] interacts with an accelerating one, resulting in a narrower energy distribution [Fig. 1(b), bottom panel]. This interaction relies on having the electron pulse duration shorter than the THz pulse cycle, such that the electron temporal phase-space distribution experiences a monotonic field [see Fig. 1(b)]. Moreover, the duration of the free-electron-THz interaction must be short enough to avoid averaging over the field.

Comparing the electron energy spectra before and at the optimal time delay shows a maximal reduction of the electron energy spread at FWHM (M) by 2.9-fold for 80 keV electron primary energy [Fig. 2(a), center panel]. Furthermore, integrating over the spectra shows that the total electron count remains constant, proving that the proposed method is indeed lossless. Significant monochromation is

also observable at other electron primary energies (Fig. 2, top and bottom rows), by a factor of 2.25 and 1.3 for 60 keV and 200 keV electrons, respectively.

Theoretical modeling of the monochromation effect can be performed using the theory of charge dynamics electron microscopy (CDEM, see also Methods). This theory has been recently applied to reconstruct the spatiotemporal profiles of photoexcited electrons and holes in InAs [38] and photoexcited electron plasma emitted from Cu [39], as well as the THz waveforms generated by these charge dynamics. The obtained theoretical results are in excellent agreement with the experimental data, as seen by the pump-probe time delay scans in Figs. 2(b) and 2(c). Further observing Figs. 2(b) and 2(c), it is evident that around $\Delta t = 0$ the opposite effect is obtained, i.e., the electron energy spread is broadened due to temporal misalignment of the electron and THz pulses.

Operating the UTEM in scanning TEM mode (low magnification STEM-EELS; see also Methods), we map the change in the electron energy spread across the lateral plane, normal to the electron propagation axis. We present the energy monochromation and mean energy shift induced by the THz near field at each point [Figs. 3(a) and 3(b), respectively]. These results show the robustness of our technique: as the interaction occurs in free space and over a relatively wide region (tens of microns), the electron beam is not trimmed or dimmed by the THz emitting structure, and the design is fairly robust to spatial misalignments of the electron-THz-field-emitter system, relative to typical fluctuations found in UTEMs. Furthermore, we observe the same monochromation effect over the extent of several hours. Moreover, the demonstrated uniformity implies that our technique does not require any dedicated electron optics, and therefore the THz emitter can be integrated at any position along the column. This is illustrated by the black circle in Figs. 3(a) and 3(b), which represents an aperture, within which we achieve high, homogeneous [i.e., same amount of monochromation, Fig. 3(a)], and isochromatic [i.e., same primary electron energy, Fig. 3(b)] energy monochromation.

Figure 3(c) shows two diffraction-plane images, taken before the pump laser pulse arrival and at the optimal electron-THz temporal overlap for monochromation. These images confirm that a small μrad -scale deflection is obtained, along with an increase in the beam angular spread, on the order of a single μrad . For practical applications these effects are completely negligible, as the typical beam convergence angle in TEM is on the order of milliradians. Moreover, in our measurement, a 50- μm size electron beam was used in proximity to the THz emitter in order to exemplify the deflection and spreading effect. In practice, one could use a much smaller (down to $\sim 5 \mu\text{m}$) beam positioned further away from the emitter, where homogeneous monochromation is obtained [Figs. 3(a) and 3(b)].

The electron sideways deflection can be estimated using momentum and impulse considerations, via the relation

$$\alpha = \frac{eE_{\perp}L/v_z}{mv_z} = \frac{1.6 \times 10^{-19} \text{ C} \times 10^3 \text{ V m}^{-1} \times 10^{-4} \text{ m}/0.5 \times 3 \times 10^8 \text{ m s}^{-1}}{9.11 \times 10^{-31} \text{ kg} \times 0.5 \times 3 \times 10^8 \text{ m s}^{-1}} \cong 1 \text{ } \mu\text{rad}, \quad (1)$$

where E_{\perp} is the transverse THz electric field amplitude (in the x - y plane), L is the electron-THz interaction length, v_z is the electron velocity along its propagation direction, and e and m are the electron charge and mass, respectively. In Eq. (1), E_{\perp} was taken to be 10^3 V m^{-1} . This value is an estimation of the THz field amplitude [38] around the single-cycle pulse null, where optimal monochromatization is obtained. The resulting angular deflection is consistent with

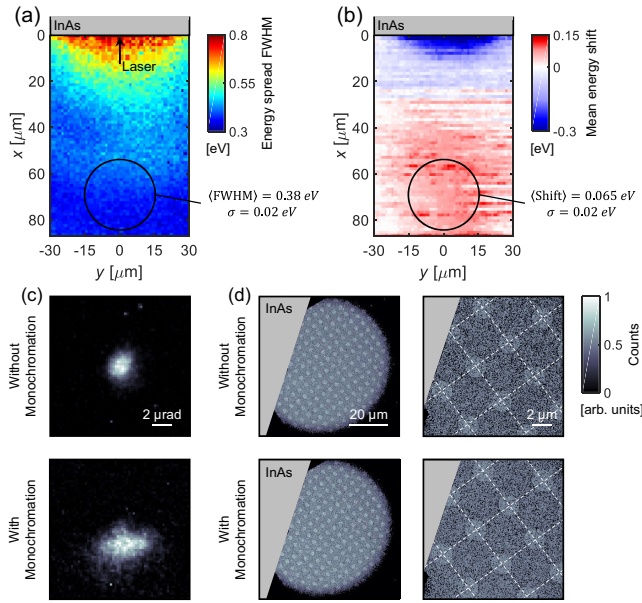


FIG. 3. In-plane spatial variation of the monochromatization effect. x - y plane maps of the electron pulse FWHM energy spread (a) and mean energy shift (b) at the time delay of optimal energy monochromatization. $x = 0$ marks the sample face (gray box) and $x > 0$ is free space. The black arrow illustrates the pump laser position on the sample face. The black circles in (a) and (b) illustrate a $30 \text{ } \mu\text{m}$ aperture located $70 \text{ } \mu\text{m}$ away from the emitter edge, inside which high and homogeneous monochromatization is achieved. The indicated values are the average and standard deviation of the energy spread FWHM and mean energy shift within the simulated aperture, respectively. (c) Diffraction plane images of the electron beam taken at a time delay without monochromatization (top) and with optimal monochromatization (bottom). A small μrad -scale deflection along with an increase in the beam angular spread are observed at the time delay of optimal monochromatization (bottom). Measuring this scale of deflection is achieved by setting the camera length to 10 m (microscope objective lens is off), and illuminating an area similar to that shown in the left panels of (d). (d) Images of a holey Carbon TEM grid placed under and adjacent to the sample (gray area), taken at the same time delays as in (c). For all data displayed in this figure the pump laser pulse energy is 10 nJ , and the electron primary energy is 80 keV .

the measured value in Fig. 3(c). Figure 3(d) shows images of a holey Carbon TEM grid placed under and adjacent to the THz emitter. The images do not display distortions due to transverse THz fields.

We investigate the energy monochromatization dependence on a variety of electron and THz pulse parameters that are readily tunable in our setup. Figure 4 displays a subset of that investigation, depicting the minimal electron energy spread versus probe electron distance from the sample x (impact parameter, panels horizontal axis), evaluated from individual STEM-EELS time-delay scans at each x position (taken at $y = 0$). We further tune the pump laser energy (main figure horizontal axis; note the change in the pump follows a power law), and observe an increase in monochromatization with increasing pump laser pulse energy. Notably, the x position of optimal monochromatization moves away from the THz emitter (larger x) with increasing pump laser pulse energy. This indicates that for a given set of parameters, there is an optimal THz power for monochromatization, which is obtained further away from the emitter when increasing the pump. At other positions, the THz field could be too strong, leading to over-rotation of the electron monochromatization is seen. Overall, the further the electron moves from the sample, the more narrowband the THz pulse becomes (centered around 0.5 THz) [38], and hence the monochromatization is more pronounced. We also modify the electron pulse initial dispersion by tuning the Wehnelt cup bias [64] at the electron gun [main figure vertical axis; see Fig. 1(a)]. This knob allows us to finely adjust the monochromator performance, at the possible expense of brightness, pulse duration, and spatial coherence.

Overall, the major limiting factors for further improving the monochromatization demonstrated in this experiment are the electron pulse phase-space parameters. These are determined by a complex combination of the electron source (tip), Wehnelt cup bias, and acceleration voltage, as well as the UV laser pulse used to pump the electron source and the nature of the photoemission process. The other limiting factor is the THz pulse cycle, which is around 2 ps in the current study. To achieve optimal monochromatization, the electron pulse should interact with a linearly varying field. This scenario is possible for a single-cycle THz pulse if the electron pulse duration is shorter than half the THz pulse cycle. This criterion is not met for 60 keV electrons ($\sim 1.5 \text{ ps}$ electron pulse duration), thereby reducing the monochromatization factor (see Fig. 2), and is barely met for the 80 keV electrons in our study ($\sim 1 \text{ ps}$ pulse duration). Control over the THz pulse frequency could be

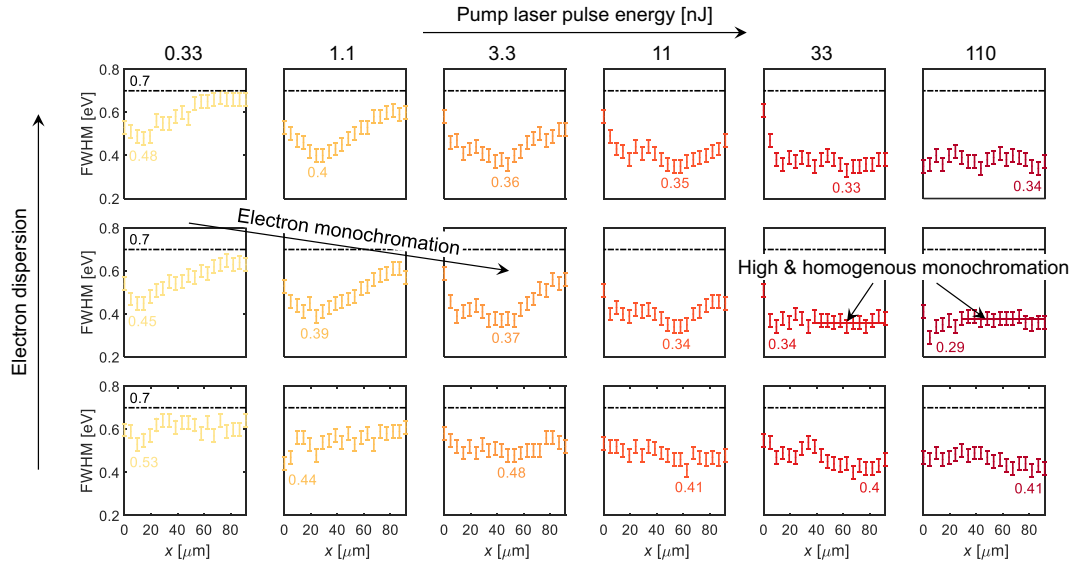


FIG. 4. Multiparameter study of the electron monochromator performance. Minimal electron energy spread (FWHM) versus impact parameter (x) for varying pump laser pulse energies (horizontal axis) and electron pulse initial dispersion (vertical axis) controlled by changing the Wehnelt cup bias. Data were obtained via one-dimensional STEM-EELS scans at $y = 0$ (see axis in Fig. 3). Electron primary energy is 80 keV. The Wehnelt setting used in the rest of our work was tuned to achieve optimal monochromation for the given parameters.

achieved by changing the type of THz emitter; single-cycle THz sources in the 0.1–10 THz range are widely available [65–67] and can further optimize our approach. The THz field can be either generated inside the UTEM or coupled from outside.

At 200 keV, the electron pulse temporal broadening (stemming from the UV laser pulse duration of ~ 200 fs) is roughly equal to the electron pulse chirp, and hence there is not much room for monochromation (the phase-space resembles a disk). Using a shorter UV laser pulse for photoemission can therefore improve the monochromator performance, specifically at high electron primary energies.

Furthermore, a higher monochromation factor could also be achieved through preshaping the electron pulse, using another point of electron-THz interaction. This approach is based on the conservation of the phase-space area (which is analogous to the conservation of emittance). The preshaping will be used to broaden the electron energy distribution by a proper selection of the electron-THz time delay, also leading to a longer pulse duration after some free-space propagation, owing to the electron pulse dispersion. The result is a flattened phase-space distribution which can then be monochromated with greater efficiency using a second point of electron-THz interaction (with a lower-frequency THz source). The output electron will have a narrower energy distribution at the expense of prolonged temporal duration.

We envision incorporating our lossless electron monochromator as an additional point of laser-electron interaction inside UTEM platforms, thus liberating the other point of interaction to conduct the experiment of choice. This modification was recently conducted in our

UTEM [68], allowing us to perform experiments with an improved electron energy resolution.

Experimental setup: The experiments are conducted using a JEOL 2100 Plus TEM equipped with a LaB₆ electron gun and driven by femtosecond laser pulses, thus operating as an UTEM, as illustrated in Fig. 1(a). In the UTEM, a laser pump pulse excites the sample, and an electron probe pulse records the sample’s transient state. The pump and probe pulses are created by a 1030 nm, ~ 220 fs laser (Carbide, Light Conversion) operating at a 1 MHz repetition rate. Each pulse is split into two: The first pulse is up-converted to UV via two stages of second-harmonic generation and then guided to the TEM cathode by an aluminum mirror inserted inside the TEM column. This process generates femtosecond electron pulses at the laser repetition rate. The electron pulses are accelerated to 60–200 keV and travel down the TEM column, passing by the vicinity of the sample and providing imaging or spectroscopic information, just as in a conventional TEM. The second pulse is converted to 800 nm wavelength and 50 fs pulse duration (FWHM) using an optical parametric amplifier (OPA) and a pulse compressor. This pulse is then used to pump the THz emitter (sample), impinging on it from the side (relative to the electron beam), where the laser spot size is 40 μm FWHM. The time delay between electron probe and laser-pump pulses is controlled by a motorized stage, thus allowing for stroboscopic measurements of femtosecond dynamics.

In our experiment, a 50-fs laser pulse is used to pump the InAs crystal, which generates the THz pulses due to the photo-Dember effect. In this case, using such a short pump laser pulse leads to stronger and more coherent THz

emission, as all the carriers inside the InAs crystal are excited in a shorter time frame. This in turn allows us to observe the monochromation effect more clearly. However, we note that the effect was also visible while using 200-fs pump laser pulses.

When using photoemission mode and optimizing for a narrow zero-loss peak, as in our experiment, our microscope operates in a regime of less than one electron per pulse on average. This number is concluded from the repetition rate of the UV pulse that is used to eject electrons from the cathode (1 MHz) compared with the total counts detected with our camera, taking into account its quantum efficiency. This situation is also common in other UTEM systems. Moreover, having effectively a single electron in the beam at any given instance is also beneficial and common to electron microscopes operating in a continuous mode, as it prevents loss of resolution due to space-charge effects.

The initially broad energy distribution of the electron pulse is attributed to (i) the uncertainty in the arrival time of the UV pulse to the cathode (UV pulse width is ~ 200 fs FWHM), (ii) the acceleration of the electron pulse in the gun, and (iii) the physics of electron photoemission from the cathode. The latter is also an active area of research, with many open questions [69–72].

Notably, the THz pulse carrier envelope phase (CEP) is locked. This can be inferred by considering our measurement scheme—measuring a specific electron-THz time delay involves the aggregation of multiple repetitions of the interaction (around 1–10 million repetitions). Since the electron pulse duration is shorter than the THz pulse envelope duration, the electron is sensitive to the carrier phase. Hence, if the CEP was not locked, during each repetition the electron would have seen different field amplitudes, and the monochromation effect could not be realized. Using the THz pulse waveforms reconstructed in Ref. [38] for 200 keV electron primary energy and 0.1–10 nJ pump laser pulse energy, while assuming a Gaussian THz pulse envelope and a carrier central frequency of 0.5 THz, we extract a CEP of 0.4–0.65 rad, depending on the pump laser pulse energy (higher pulse energy corresponds to larger CEP).

Electron spectroscopy in STEM-EELS mode: To analyze the electron (kinetic energy) spectrum after interaction with the sample, a postcolumn EELS system manufactured by Gatan is installed in the TEM. The EELS data can be captured at each x - y (lateral) position within the field of view (FOV) using the built-in scanning TEM (STEM) capability (Figs. 3 and 4). The results presented in Figs. 3(a) and 3(b) are acquired with a FOV of $85 \times 60 \mu\text{m}^2$ and an electron lateral spot size of $1 \mu\text{m}$ FWHM. The STEM electron lens system is tuned to collimate the electron, so it maintains this spot size along the entire length of the interaction region.

In order to collect the data shown in Figs. 3 and 4, the STEM-EELS measurement is repeated for several pump-probe time delays (Figs. 3 and 4), pump laser pulse

energy, and electron dispersion (Fig. 4), generating a multidimensional hypercube of EELS data.

Sample preparation: The sample used in our experiments was prepared from a p-type (10^{17} cm^{-3}) 500 μm -thick single crystal InAs wafer with (111) growth orientation (from MTI Corp.). A piece from the wafer was manually thinned and polished to 60 μm using standard TEM sample preparation techniques. The thinned crystal was then cleaved along the {110} planes and glued to a TEM copper grid before being mounted on the TEM holder.

Sample damage: Examining the InAs crystal surface after the experiments were carried out (using an optical microscope at $\times 100$ magnification), we did not observe any laser-induced damage even after using 110 nJ pulses. Furthermore, we did not observe any degradation in the crystal THz-generation performance. Each pump laser pulse energy was applied to the crystal for at least one hour for data collection.

Considerations for THz emitter selection: InAs was chosen as the THz emitter owing to its strong and robust THz emission characteristics, with a central frequency roughly matching the electron pulse duration. Moreover, using a crystal is technically simpler than using THz emitting electro-optical devices (such as photoconductive emitters), which require the introduction of electrical wiring into the microscope column. *In situ* THz generation using InAs is also technically simpler than using an external THz source, which necessitates additional optics to guide, couple in, and focus the THz pulse into the microscope column. This approach also requires the incorporation of some THz-reflecting media or a THz resonator at the point of electron-THz interaction to enhance the interaction strength.

However, an InAs crystal has its own disadvantages. For example, InAs in the mentioned configuration does not allow for frequency tuning of the generated THz field, which could have helped match the electron pulse duration at different primary electron energies for more efficient monochromation.

Classical description of CDEM: In this section we provide a classical theoretical framework for the THz-electron interaction in the UTEM. Such a formalism is adequate to understand the results of our work. A more general formalism, also considering a quantum-mechanical treatment of the electron wavefunction and the conditions for using classical versus quantum treatment is derived in Refs. [38,39].

Given that the observed electron energy spectrum can be understood using the classical work done by the fields on a point charge, it is of interest to develop a purely classical theory of CDEM. The classical theory amounts to (1) calculating the EM fields that act on the impinging electrons (this step is shared with the quantum theory), (2) calculating the classical work done on the electron, and (3) averaging over the initial electron distribution to get the statistics of energy loss that is experimentally probed. For the latter, the distribution refers to the electron pulse duration, which

determines a variance in the electron arrival time, as well as the electron energy width, which broadens the measured energy spectrum.

In order to evaluate the electron energy shift in the classical limit, one must first find the electric and magnetic fields resulting from the above potentials:

$$\mathbf{E} = -\nabla\Phi - \frac{\partial\mathbf{A}}{\partial t}, \quad \mathbf{B} = \nabla \times \mathbf{A}. \quad (2)$$

We next calculate the Lorentz force generated by the fields:

$$\mathbf{F} = -e(\mathbf{E} + \mathbf{v} \times \mathbf{B}). \quad (3)$$

Defining the electron trajectory along z as

$$z(t) = z_0 + v_z(t - \Delta t), \quad (4)$$

the mean electron energy shift is then given by

$$\Delta\bar{\mathcal{E}}(\Delta t) = \int_{t_i}^{t_f} \mathbf{F} \cdot \mathbf{v} dt = \int_{z_i}^{z_f} F_z dz, \quad (5)$$

where in the rightmost expression, the paraxiality assumption has been applied, implying that the electron velocity is directed exclusively along z . Moreover, the influence of the magnetic field in our experiment can be neglected since the system characteristic dimension (L) is considerably smaller than the THz wavelength ($L \cong 10 \mu\text{m} \ll \lambda_{\text{THz}} \cong 600 \mu\text{m}$). Therefore, we are left with

$$F_z = -eE_z, \quad E_z = -\frac{\partial\Phi}{\partial z} - \frac{\partial A_z}{\partial t}. \quad (6)$$

We note that, relying on the photo-Dember effect, the THz polarization in our experiments is determined by the photogenerated electron-hole distribution inside the InAs crystal, which forms a dipole structure with a dipole moment oriented into the bulk (i.e., along x). The THz near field therefore has a dipolelike pattern, the polarization of which is fixed in all of our measurements. Changes in the electron energy distribution (acceleration and/or monochromation) can be induced only by the THz field component along its trajectory (E_z).

Based on extensive simulations and parameter fitting using a hydrodynamic model of the photo-Dember effect [38], we estimate the THz pulse peak field strength to be in the range of 10^4 to 10^6 V m^{-1} , depending on the pump laser pulse energy used. As mentioned before, for ideal monochromation, the electron interacts with the THz pulse around its null, where the field strength is considerably lower (in the range of 10^3 to 10^4 V m^{-1}).

In the final step of the calculation, the mean electron energy shift $\Delta\bar{\mathcal{E}}$ is represented in energy-shift and time-delay space using a sum of delta functions:

$$\Delta\bar{\mathcal{E}}(\Delta t, \Delta\mathcal{E}) = \sum_i \delta(\Delta t - \Delta t_i, \Delta\mathcal{E} - \Delta\bar{\mathcal{E}}(\Delta t_i)). \quad (7)$$

More explicitly, for each time delay Δt_i , the electron undergoes a certain energy shift $\Delta\bar{\mathcal{E}}(\Delta t_i)$, evaluated from Eq. (5). This integral gives a scalar result which can then be represented in the two-dimensional energy-shift and time-delay space using the delta function $\delta(\Delta t - \Delta t_i, \Delta\mathcal{E} - \Delta\bar{\mathcal{E}}(\Delta t_i))$. To obtain the entire time-delay scan, a summation over a range of time delays is then performed. This expression is then convoluted in energy-shift ($\Delta\mathcal{E}$) and time-delay (Δt) space with an incoherent broadening function—a two-dimensional chirped Gaussian of the form

$$\exp(-a\Delta t^2 - 2b\Delta t\Delta\mathcal{E} - c\Delta\mathcal{E}^2), \quad (8)$$

thus, reproducing the EELS spectra observed in the experiment. The chirp b is added here to accommodate for the electron pulse dispersion, resulting from the electron emission process and free-space propagation inside the TEM column. The parameters (a, b, c) can be obtained experimentally, through fitting the above chirped Gaussian to one of the energy sidebands obtained in a photon-induced near-field electron microscopy experiment [6,7,73], conducted by replacing the THz emitter with an aluminum foil sample. For the 80 keV fit presented in Fig. 2(c), these parameters are $a = 110 \text{ ps}^{-2}$, $b = 80 \text{ ps}^{-1} \text{ eV}^{-1}$, $c = 70 \text{ eV}^{-2}$.

The research was supported by the European Research Council (ERC Starting Grant No. 851780-NanoEP), the European Union Horizon 2020 Research and Innovation Program (Grant Agreement No. 964591 SMART-electron and No. 101101048-ERC-POC), and the Israel Innovation Authority (Grant Agreement No. 77140 Nofar). The experiments were performed on the UTEM of the AdQuanta group of I. K., which is installed in the electron microscopy center (MIKA) of the Department of Materials Science and Engineering at Technion. M. Y. and R. D. are partially supported by the VATAT Quantum Science and Technology scholarship.

*These authors contributed equally to this work.

†kaminer@technion.ac.il

- [1] R. F. Egerton, *Electron Energy-Loss Spectroscopy in the Electron Microscope* (Springer Science & Business Media, USA, 2011), 10.1007/978-1-4419-9583-4.
- [2] O. L. Krivanek *et al.*, Progress in ultrahigh energy resolution EELS, *Ultramicroscopy* **203**, 60 (2019).
- [3] A. H. Zewail, Four-dimensional electron microscopy, *Science* **328**, 187 (2010).
- [4] L. Piazza, D. J. Masiel, T. LaGrange, B. W. Reed, B. Barwick, and F. Carbone, Design and implementation of a fs-resolved transmission electron microscope based on thermionic gun technology, *Chem. Phys.* **423**, 79 (2013).

- [5] A. Feist *et al.*, Ultrafast transmission electron microscopy using a laser-driven field emitter: Femtosecond resolution with a high coherence electron beam, *Ultramicroscopy* **176**, 63 (2017).
- [6] B. Barwick, D. J. Flannigan, and A. H. Zewail, Photon-induced near-field electron microscopy, *Nature (London)* **462**, 902 (2009).
- [7] S. T. Park, M. Lin, and A. H. Zewail, Photon-induced near-field electron microscopy (PINEM): Theoretical and experimental, *New J. Phys.* **12**, 123028 (2010).
- [8] L. Piazza, T. T. A. Lummen, E. Quiñonez, Y. Murooka, B. W. Reed, B. Barwick, and F. Carbone, Simultaneous observation of the quantization and the interference pattern of a plasmonic near-field, *Nat. Commun.* **6**, 6407 (2015).
- [9] T. T. A. Lummen, R. J. Lamb, G. Berruto, T. Lagrange, L. Dal Negro, F. J. García de Abajo, D. McGrouther, B. Barwick, and F. Carbone, Imaging and controlling plasmonic interference fields at buried interfaces, *Nat. Commun.* **7**, 13156 (2016).
- [10] D. R. Cremons, D. A. Plemmons, and D. J. Flannigan, Femtosecond electron imaging of defect-modulated phonon dynamics, *Nat. Commun.* **7**, 11230 (2016).
- [11] A. Ryabov and P. Baum, Electron microscopy of electromagnetic waveforms, *Science* **353**, 374 (2016).
- [12] N. Talebi, Interaction of electron beams with optical nanostructures and metamaterials: From coherent photon sources towards shaping the wave function, *J. Opt.* **19**, 103001 (2017).
- [13] Y. Morimoto and P. Baum, Diffraction and microscopy with attosecond electron pulse trains, *Nat. Phys.* **14**, 252 (2018).
- [14] O. Kfir, H. Lourenço-Martins, G. Storeck, M. Sivis, T. R. Harvey, T. J. Kippenberg, A. Feist, and C. Ropers, Controlling free electrons with optical whispering-gallery modes, *Nature (London)* **582**, 46 (2020).
- [15] K. Wang, R. Dahan, M. Shentcis, Y. Kauffmann, A. Ben Hayun, O. Reinhardt, S. Tsesses, and I. Kaminer, Coherent interaction between free electrons and a photonic cavity, *Nature (London)* **582**, 50 (2020).
- [16] X. Fu *et al.*, Nanoscale-femtosecond dielectric response of Mott insulators captured by two-color near-field ultrafast electron microscopy, *Nat. Commun.* **11**, 5770 (2020).
- [17] A. Ryabov, J. W. Thurner, D. Nabben, M. V. Tsarev, and P. Baum, Attosecond metrology in a continuous-beam transmission electron microscope, *Sci. Adv.* **6**, eabb1393 (2020).
- [18] Y. Kurman *et al.*, Spatiotemporal imaging of 2D polariton wave packet dynamics using free electrons, *Science* **372**, 1181 (2021).
- [19] T. Danz, T. Domröse, and C. Ropers, Ultrafast nanoimaging of the order parameter in a structural phase transition, *Science* **371**, 371 (2021).
- [20] A. Konečná, J. Li, J. H. Edgar, F. J. García de Abajo, and J. A. Hachtel, Revealing nanoscale confinement effects on hyperbolic phonon polaritons with an electron beam, *Small* **17**, 2103404 (2021).
- [21] X. Li, G. Haberfehlner, U. Hohenester, O. Stéphan, G. Kothleitner, and M. Kociak, Three-dimensional vectorial imaging of surface phonon polaritons, *Science* **371**, 1364 (2021).
- [22] J. K. El-Demellawi, S. Lopatin, J. Yin, O. F. Mohammed, and H. N. Alshareef, Tunable multipolar surface plasmons in 2D $\text{Ti}_3\text{C}_2\text{T}_x$ MXene flakes, *ACS Nano* **12**, 8485 (2018).
- [23] A. B. Yankovich, B. Munkhbat, D. G. Baranov, J. Cuadra, E. Olsén, H. Lourenço-Martins, L. H. G. Tizei, M. Kociak, E. Olsson, and T. Shegai, Visualizing spatial variations of plasmon-exciton polaritons at the nanoscale using electron microscopy, *Nano Lett.* **19**, 8171 (2019).
- [24] V. Mkhitarian *et al.*, Can copper nanostructures sustain high-quality plasmons?, *Nano Lett.* **21**, 2444 (2021).
- [25] Y. Auad, C. Hamon, M. Tencé, H. Lourenço-Martins, V. Mkhitarian, O. Stéphan, F. J. García de Abajo, L. H. G. Tizei, and M. Kociak, Unveiling the coupling of single metallic nanoparticles to whispering-gallery microcavities, *Nano Lett.* **22**, 319 (2022).
- [26] L. H. G. Tizei, Y. C. Lin, M. Mukai, H. Sawada, A. Y. Lu, L. J. Li, K. Kimoto, and K. Suenaga, Exciton mapping at subwavelength scales in two-dimensional materials, *Phys. Rev. Lett.* **114**, 107601 (2015).
- [27] A. Kogar *et al.*, Signatures of exciton condensation in a transition metal dichalcogenide, *Science* **358**, 1314 (2017).
- [28] O. L. Krivanek *et al.*, Vibrational spectroscopy in the electron microscope, *Nature (London)* **514**, 209 (2014).
- [29] C. Dwyer, T. Aoki, P. Rez, S. L. Y. Chang, T. C. Lovejoy, and O. L. Krivanek, Electron-beam mapping of vibrational modes with nanometer spatial resolution, *Phys. Rev. Lett.* **117**, 256101 (2016).
- [30] M. J. Lagos, A. Trügler, U. Hohenester, and P. E. Batson, Mapping vibrational surface and bulk modes in a single nanocube, *Nature (London)* **543**, 529 (2017).
- [31] F. S. Hage, R. J. Nicholls, J. R. Yates, D. G. McCulloch, T. C. Lovejoy, N. Dellby, O. L. Krivanek, K. Refson, and Q. M. Ramasse, Nanoscale momentum-resolved vibrational spectroscopy, *Sci. Adv.* **4**, eaar7495 (2018).
- [32] J. A. Hachtel, J. Huang, I. Popovs, S. Jansone-Popova, J. K. Keum, J. Jakowski, T. C. Lovejoy, N. Dellby, O. L. Krivanek, and J. Carlos Idrobo, Identification of site-specific isotopic labels by vibrational spectroscopy in the electron microscope, *Science* **363**, 525 (2019).
- [33] F. S. Hage, D. M. Kepaptsoglou, Q. M. Ramasse, and L. J. Allen, Phonon spectroscopy at atomic resolution, *Phys. Rev. Lett.* **122**, 016103 (2019).
- [34] S. M. Collins, D. M. Kepaptsoglou, J. Hou, C. W. Ashling, G. Radtke, T. D. Bennett, P. A. Midgley, and Q. M. Ramasse, Functional group mapping by electron beam vibrational spectroscopy from nanoscale volumes, *Nano Lett.* **20**, 1272 (2020).
- [35] F. S. Hage, G. Radtke, D. M. Kepaptsoglou, M. Lazzeri, and Q. M. Ramasse, Single-atom vibrational spectroscopy in the scanning transmission electron microscope, *Science* **367**, 1124 (2020).
- [36] L. H. G. Tizei *et al.*, Tailored nanoscale plasmon-enhanced vibrational electron spectroscopy, *Nano Lett.* **20**, 2973 (2020).
- [37] G. Hergert, A. Wöste, J. Vogelsang, T. Quenzel, D. Wang, P. Gross, and C. Lienau, Probing transient localized electromagnetic fields using low-energy point-projection electron microscopy, *ACS Photonics* **8**, 2573 (2021).

- [38] M. Yannai *et al.*, Ultrafast electron microscopy of nanoscale charge dynamics in semiconductors, *ACS Nano* **17**, 3645 (2023).
- [39] I. Madan *et al.*, Charge dynamics electron microscopy: Nanoscale imaging of femtosecond plasma dynamics, *ACS Nano* **17**, 3657 (2023).
- [40] O. Kfir, Entanglements of electrons and cavity photons in the strong-coupling regime, *Phys. Rev. Lett.* **123**, 103602 (2019).
- [41] V. Di Giulio, M. Kociak, and F. J. García de Abajo, Probing quantum optical excitations with fast electrons, *Optica* **6**, 1524 (2019).
- [42] A. Gorlach, A. Karnieli, R. Dahan, E. Cohen, A. Pe'er, and I. Kaminer, Ultrafast non-destructive measurement of the quantum state of light using free electrons, *arXiv*: 2012.12069.
- [43] R. Dahan *et al.*, Imprinting the quantum statistics of photons on free electrons, *Science* **373**, 1324 (2021).
- [44] Y. Adiv *et al.*, Observation of 2D Cherenkov Radiation, *Phys. Rev. X* **13**, 011002 (2023).
- [45] F. Houdellier, G. M. Caruso, S. Weber, M. Kociak, and A. Arbouet, Development of a high brightness ultrafast transmission electron microscope based on a laser-driven cold field emission source, *Ultramicroscopy* **186**, 128 (2018).
- [46] R. Shiloh *et al.*, Miniature light-driven nanophotonic electron acceleration and control, *Adv. Opt. Photonics* **14**, 862 (2022).
- [47] Y. Morimoto, Attosecond electron-beam technology: A review of recent progress, *Microscopy* **72**, 2 (2023).
- [48] L. C. Oldfield, A rotationally symmetric electron beam chopper for picosecond pulses, *J. Phys. E* **9**, 455 (1976).
- [49] T. Hosokawa, H. Fujioka, and K. Ura, Gighertz stroboscopy with the scanning electron microscope, *Rev. Sci. Instrum.* **49**, 1293 (1978).
- [50] A. Lassise, P. H. A. Mutsaers, and O. J. Luiten, Compact, low power radio frequency cavity for femtosecond electron microscopy, *Rev. Sci. Instrum.* **83**, 043705 (2012).
- [51] J. Qiu, G. Ha, C. Jing, S. V. Baryshev, B. W. Reed, J. W. Lau, and Y. Zhu, GHz laser-free time-resolved transmission electron microscopy: A stroboscopic high-duty-cycle method, *Ultramicroscopy* **161**, 130 (2016).
- [52] J. F. M. van Rens, W. Verhoeven, E. R. Kieft, P. H. A. Mutsaers, and O. J. Luiten, Dual mode microwave deflection cavities for ultrafast electron microscopy, *Appl. Phys. Lett.* **113**, 163104 (2018).
- [53] I. G. C. Weppelman, R. J. Moerland, J. P. Hoogenboom, and P. Kruit, Concept and design of a beam blanker with integrated photoconductive switch for ultrafast electron microscopy, *Ultramicroscopy* **184**, 8 (2018).
- [54] C. Kealhofer, W. Schneider, D. Ehberger, A. Ryabov, F. Krausz, and P. Baum, All-optical control and metrology of electron pulses, *Science* **352**, 429 (2016).
- [55] D. Ehberger, C. Kealhofer, and P. Baum, Electron energy analysis by phase-space shaping with THz field cycles, *Struct. Dyn.* **5**, 044303 (2018).
- [56] D. Ehberger, K. J. Mohler, T. Vasileiadis, R. Ernstorfer, L. Waldecker, and P. Baum, Terahertz Compression of Electron Pulses at a Planar Mirror Membrane, *Phys. Rev. Appl.* **11**, 024034 (2019).
- [57] R. K. Li *et al.*, Terahertz-based subfemtosecond metrology of relativistic electron beams, *Phys. Rev. Accel. Beams* **22**, 012803 (2019).
- [58] L. Wimmer, G. Herink, D. R. Solli, S. V. Yalunin, K. E. Echternkamp, and C. Ropers, Terahertz control of nanotip photoemission, *Nat. Phys.* **10**, 432 (2014).
- [59] E. A. Nanni, W. R. Huang, K. H. Hong, K. Ravi, A. Fallahi, G. Moriena, R. J. Dwayne Miller, and F. X. Kärtner, Terahertz-driven linear electron acceleration, *Nat. Commun.* **6**, 8486 (2015).
- [60] E. Curry, S. Fabbri, J. Maxson, P. Musumeci, and A. Gover, Meter-scale terahertz-driven acceleration of a relativistic beam, *Phys. Rev. Lett.* **120**, 094801 (2018).
- [61] D. Zhang *et al.*, Segmented terahertz electron accelerator and manipulator (STEAM), *Nat. Photonics* **12**, 336 (2018).
- [62] C. J. R. Duncan, D. A. Muller, and J. M. Maxson, Lossless Monochromation for Electron Microscopy with Pulsed Photoemission Sources and Radio-Frequency Cavities, *Phys. Rev. Appl.* **14**, 014060 (2020).
- [63] H. Dember, Photoelectromotive force in cuprous oxide crystals, *Phys. Z.* **32**, 554 (1931).
- [64] D. B. Williams and C. B. Carter, *Transmission Electron Microscopy: A Textbook for Materials Science* (Springer, New York, 2009), 10.1007/978-0-387-76501-3.
- [65] M. Tonouchi, Cutting-edge terahertz technology, *Nat. Photonics* **1**, 97 (2007).
- [66] R. A. Lewis, A review of terahertz sources, *J. Phys. D* **47**, 374001 (2014).
- [67] J. A. Fülöp, S. Tzortzakis, and T. Kampfrath, Laser-driven strong-field terahertz sources, *Adv. Opt. Mater.* **8**, 1900681 (2020).
- [68] <https://www.smartelectron.eu>.
- [69] C. Ropers, D. R. Solli, C. P. Schulz, C. Lienau, and T. Elsaesser, Localized multiphoton emission of femtosecond electron pulses from metal nanotips, *Phys. Rev. Lett.* **98**, 043907 (2007).
- [70] M. Krüger, M. Schenk, and P. Hommelhoff, Attosecond control of electrons emitted from a nanoscale metal tip, *Nature (London)* **475**, 78 (2011).
- [71] H. Y. Kim, M. Garg, S. Mandal, L. Seiffert, T. Fennel, and E. Goulielmakis, Attosecond field emission, *Nature (London)* **613**, 662 (2023).
- [72] O. Bhorade, B. Deconihout, I. Blum, S. Moldovan, J. Houard, A. Normand, K. Jagtap, M. More, and A. Vella, Bright and ultrafast electron point source made of LaB₆ nanotip, *Nanoscale Adv.* **5**, 2462 (2023).
- [73] F. J. García de Abajo, A. Asenjo-García, and M. Kociak, Multiphoton absorption and emission by interaction of swift electrons with evanescent light fields, *Nano Lett.* **10**, 1859 (2010).